Journal of Infrastructure Preservation and Resilience

RESEARCH Open Access

A novel random finite element model for holistically modeling of the frost effects on soils and cold region pavements

Shaoyang Dong[1†], Yusheng Jiang[1†] and Xiong Yu[2*]

Abstract

This paper describes the development of a random finite element model (RFEM) that allows holistic simulation of frozen soil behaviors, including the effects of phase transition and the consequent internal stress and volume changes. The performance of the model is firstly validated with laboratory experiments. The model is implemented to simulate the effects of frost action on pavement. The coupled thermal-mechanical actions including the mechanical responses of subgrade soils subjected to freezing temperature and its effects on the pavement structure are analyzed. The results show that the frost action and expansion of ice lenses change the interaction modes between pavement layers. This leads to increase of stress and deformation in the pavement layer. Methods to mitigate the effects of frost heave are analyzed with this model. The simulation results indicate that the detrimental effects of frost heave on the pavement structure can be mitigated by increasing the thickness of base layer, use of thermal insulation layer or improve drainage in the subgrade layer. The RFEM combines the advantages of discrete element model (DEM) in holistically describing the microstructure effects and in the finite element model (FEM) in terms of computational efficiency. This allows to focus research on understanding the behaviors of individual soils phase and their interfacial interactions.

Keywords: Random finite element model, Finite element model, Frozen soil, Frost heave, Cold region pavement, Climate resilience

Introduction

Frost heave in the cold climate region may cause serious damage to the pavement infrastructure [1–6]. The resulting cracks, dips, heaving and potholes make driving uncomfortable, damage our vehicles and increase the risk of car accidents [3]. It is costly and take huge amount of highway budgets to repair the damaged pavement. Three basic factors work together to generate frost heave: 1) freezing temperatures; 2) frost susceptible soils (such as silty soils or clayey soils); 3) water in the subgrade soils [7]. Frost heave of soils is a complex coupled multi-physical process involving the coupling of the thermal-hydro-mechanical (THM) field [8–14]. The THM process is coupled by extension of soil mechanics under isothermal conditions to incorporate the effects due to thermal expansion of solid skeleton as well as the pore fluid migration [15, 16]. Methods for mitigating the frost heave in pavement include increasing the thickness of the base layer, insulate the subgrade soil and drain water in the subgrade to the sides [17–19].

The frost heave is mainly caused by the formation of ice lenses. The first widely accepted theory for explaining the ice lens formation is the capillary theory which states that water is draw by the matric suction upwards

†Shaoyang Dong and Yusheng Jiang contributed equally to this work.

†Shaoyang Dong and Yusheng Jiang are co-first authors.

*Correspondence: xxy21@case.edu

[2] Opal J. and Richard A. Vanderhoof Professor and Chair, Department of Civil and Environmental Engineering, Professor of Electrical Engineering and Computer Science, Case Western Reserve University, Cleveland, OH, USA
Full list of author information is available at the end of the article

to form the ice lenses [20]. The drawback for the capillary theory is that it could not account for the initiation of new ice lenses. Another model to explain the ice lens formation is the frost fringe model which proposes that frost heave can occur after ice has formed a frozen fringe by penetrating into the pores of the soil [21]. The particle-engulfment model and geometrical supercooling model are recently developed models to simulate the periodic formation of ice lenses that observed in the experiment [22].

The thermal, hydraulic, and mechanical properties of soil are highly variable and are affected by the soil microstructure as well as soil phase distributions. The soil phases (e.g., soil particle, water, and air) are randomly distributed throughout the soil sample due to complex geological processes. This random characteristic can be described by the random-finite element method (RFEM) [23–26]. These properties may include parameters such as Young's modulus, Poisson's ratio, density, thermal conductivity, heat capacity, coefficient of thermal expansion and a variety of other parameters [27, 28]. The RFEM is an extension of the traditional FEM that adds randomness to material properties. Fenton et al. [28] combined random field simulation with the nonlinear finite element method to investigate the active earth pressure and stability of the retaining wall. Luo and Bathurst [29] performed probabilistic stability analyses for reinforced slopes using RFEM. Selmi et al. [30] studied the probabilistic failure envelopes of skirted foundations based on RFEM.

In the microstructural view, frozen soil is a four-phase material that includes soil particles, ice, water, and air, arranged randomly due to complex geological processes [31]. Researchers have built a microstructural model for soil [32, 33]. Tracy et al. [34] and Helliwell et al. [35] obtained the structure of soil by using X-ray Computed Tomography (CT) images. The microstructure extracted from the high-resolution images provides a foundation for simulating the physical coupling process, which could improve the understanding of THM coupled physics at a multiscale, i.e. micro-scale or pore-scale of soil samples. This paper describes the development and implementation of random finite element model for the multiphysics thermo-mechanical process in the subgrade frozen soils of a pavement. The spatial randomness of soil parameters is described with this model. The results unveil interesting phenomena due to the soil microstructure.

Theoretical basis

The theoretical basis for the thermo-hydro-mechanical processes has been established in the past years. Three types of physical fields (thermal field, hydraulic field, and mechanical field) are modelled with continuum mechanics and the mixture theory to describe the fundamental conservation principles. The theoretical basis for the random FEM model involving multiple phases is summarized in the following. It is noted that an annotation α is used to represents the phase type, which can be *s*, *i*, *w*, *a* that represents solid particle, ice, water and air, respectively. For example, the partial mass density of each phase is denoted by ρ^{α}, and intrinsic mass density of each phase is given by ρ_{α}. The symbol ϕ is used to represent the volumetric fraction of the specific phase.

Equation (1) represents the volumetric content of phases in frozen soil, i.e.,

$$\sum \phi^{\alpha} = 1 \text{or } \phi^{\mathrm{s}} + \phi^{\mathrm{i}} + \phi^{\mathrm{w}} + \phi^{\mathrm{a}} = 1 \tag{1}$$

The partial mass density is related to the intrinsic mass density of each phase via

$$\rho^{\alpha} = \varnothing^{\alpha} \rho_{\alpha} \tag{2}$$

Therefore,

$$\sum \rho^{\alpha} = \sum \varnothing^{\alpha} \rho_{\alpha} = \rho \tag{3}$$

where ρ is the total mass density of the frozen soil.

The mass conservation equations for each of the four phases (solid particle, ice, water and air) considering the compressibility, motion, and flow, is described by the following equations:

$$\frac{\mathrm{d}\phi^{\mathrm{s}}}{\mathrm{dt}} + \frac{\phi^{s}}{K_s}\frac{\mathrm{dp_s}}{\mathrm{dt}} + \phi^{s}\,\mathrm{div}\,(v_s) = 0 \tag{4}$$

$$\frac{\mathrm{d}\phi^{\mathrm{i}}}{\mathrm{dt}} + \frac{\phi^{i}}{K_i}\frac{\mathrm{dp_i}}{\mathrm{dt}} + \phi^{i}\,\mathrm{div}\,(v_s) = 0 \tag{5}$$

$$\frac{\mathrm{d}\phi^{w}}{dt} + \frac{\phi^{w}}{K_w}\frac{\mathrm{d}p_w}{dt} + \phi^{w}\,\mathrm{div}\,(v_s) = -\frac{1}{\rho_w}\,\mathrm{div}\,\left(\phi^{w}\rho_w(v_w\text{-}v_s)\right) \tag{6}$$

$$\frac{\mathrm{d}\phi^{a}}{dt} + \frac{\phi^{a}}{K_a}\frac{\mathrm{d}p_a}{dt} + \phi^{a}\,\mathrm{div}\,(v_s) = -\frac{1}{\rho_a}\,\mathrm{div}\,\left(\phi^{a}\rho_a(v_a\text{-}v_s)\right) \tag{7}$$

where K_s, K_i, K_w and K_a are the bulk modulus of solid particle, ice, water and air, respectively; p_s, p_i, p_w and p_a are the intrinsic pressures on the solid particle, ice, water and air, respectively; v_s, v_w and v_a are the velocity of the solid particle, water and air, respectively. In this study, the solid phase and ice are considered incompressible.

The governing equation for the thermal fields (Eq. 8) contains the convection and conduction terms and is modified from the Fourier's equation.

$$\rho_\alpha C_{p_\alpha} \frac{\partial T}{\partial t} + \rho_\alpha C_{p_\alpha} q \cdot \nabla T = \nabla \cdot (k_\alpha \nabla T) \tag{8}$$

where $C_{p\alpha}$ is the heat capacity; k_α is the thermal conductivity; T is the temperature and q is the flux. The effects of latent heat associated with phase change (i.e., water to ice or ice to water) is treated as equivalent heat capacity over a prescribed temperature range around the phase transition temperature.

The flow of moisture is described with the Darcy's law (Eq. 9):

$$q = -\frac{\kappa_\alpha}{\mu} \nabla p \tag{9}$$

where p is the pore-water pressure; μ is the dynamic viscosity and q is the flux of reference fluid flow. It is noted κ_α is the intrinsic permeability of the reference fluid (water in this study) across the individual phase. The effects of freezing or thawing on the bulk hydraulic properties are accounted for by the corresponding volume and arrangement of individual phase.

The governing equation for the mechanical field is the Navier's equation, which includes strain-displacement correlation (Eq. 10), the constitutive relationship (Eq. 11) and the equation of motion (Eq. 12).

The strain-displacement correlation for individual phase is

$$\varepsilon_\alpha = \frac{1}{2}\left[\nabla \mathrm{u}_\alpha + (\nabla \mathrm{u}_\alpha)^T\right] \tag{10}$$

where ε_α is the strain tensor; u_α is the displacement vector.

The constitutive relationship for individual phase is

$$\sigma^\alpha = D^\alpha \left(\varepsilon^\alpha - \varepsilon_0^\alpha - \varepsilon_{th}^\alpha - \varepsilon_{hp}\right) + \sigma_0^\alpha \tag{11}$$

where D^α is the stiffness matrix of the corresponding phase of soil skeleton; σ^α is the stress tensor; ${\sigma^\alpha}_0$ is the initial stress tensor; ε^α is the total strain tensor; ${\varepsilon^\alpha}_0$ is the initial strain; ${\varepsilon^\alpha}_{th}$ is the strain caused by thermal expansion; ε_{hp} is the strain caused by the change of matric suction.

The equation of motion is

$$\nabla \cdot (\mathrm{C}_\alpha \nabla \mathrm{u}_\alpha) + \mathrm{F} = \rho_\alpha \&_\alpha \tag{12}$$

where C_α is the stiffness tensor of the material and F is the body force.

The equation for the thermal expansion is:

$${\varepsilon^\alpha}_{th} = \beta_\alpha \left(T - T_{ref}\right) \tag{13}$$

where β_α is coefficient of thermal expansion; T is temperature; and T_{ref} is the reference temperature.

In this study, the above governing equations are applied to a geometry with randomly generated phases. For each phase, the same governing equations forms are applied and solved by finite element method via software. However, the material-based parameters (e.g., thermal conductivity, heat capacity, material density) in these governing equations are different for each phase. These parameters are determined and assigned by the specific phase.

Measurements of the mechanical and thermal behaviors during freezing and thawing processes

Two identical cylindered silt specimens of 33 mm in diameter and 72 mm in height were prepared with Harvard miniature compactor. The specimens have a gravimetric water content of 22% and dry density of 1.708 g/cm^3. The initial temperature is 20 degrees Celsius. The specimens were thermally insulated on sides and at the bottom so that only the top surface is exposed to create thermal flow mainly along vertical direction. The wrapped specimens were placed in the freezer with a temperature of −20 degrees Celsius. Thermocouples were installed in the silt specimen at the location of 10 mm, 30 mm and 50 mm from top of the specimen to measure the temperature distribution along the silt specimens during the freezing process. Two different methods are utilized to measure the vertical deformations of the specimens during the freezing process, which include manual measurement with dial gauge indicator and automatic measurement with a laser displacement transducer (Fig. 1). The performance of these methods are compared from the measurement on two separate specimens.

The laser displacement transducer and the thermocouples were connected to the computer to monitor and record the vertical deformation and temperature distribution in the soil specimens during the freezing and thawing process. The vertical strains and the temperature distribution of the silt specimen 1 during the first cycle freezing process are plotted in Fig. 2a and Fig. 3a, respectively. The specimen 2 was placed in the freezer until it is completely frozen. Subsequently, it was taken out of the freezer and subjected to the thawing process with a temperature of 19 degrees Celsius. Figure 2b compares the measured vertical strain during the first cycle thawing process.

For the silt specimen No. 1 measured by the indicator during the freezing process, the vertical strain decreased from 0 to −0.007 in the first half hour, possibly due to the compaction of soil at increasing matric suction, then the vertical strain of the specimen increased from −0.007 to 0.005 for the rest of the time due to frost heave. Similar trend of volume change was observed by use of the laser displacement transducer for the silt specimen No. 1. The vertical strain decreased from 0 to −0.0065 in the first 35 minutes

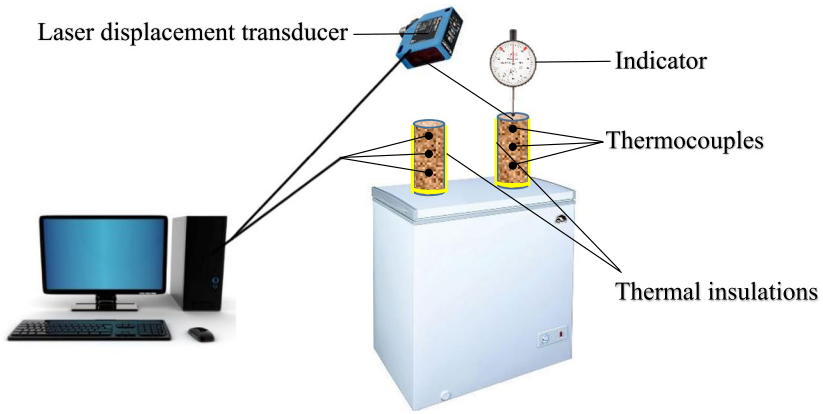

Fig. 1 The schematic picture of the experimental system measuring the frozen soil

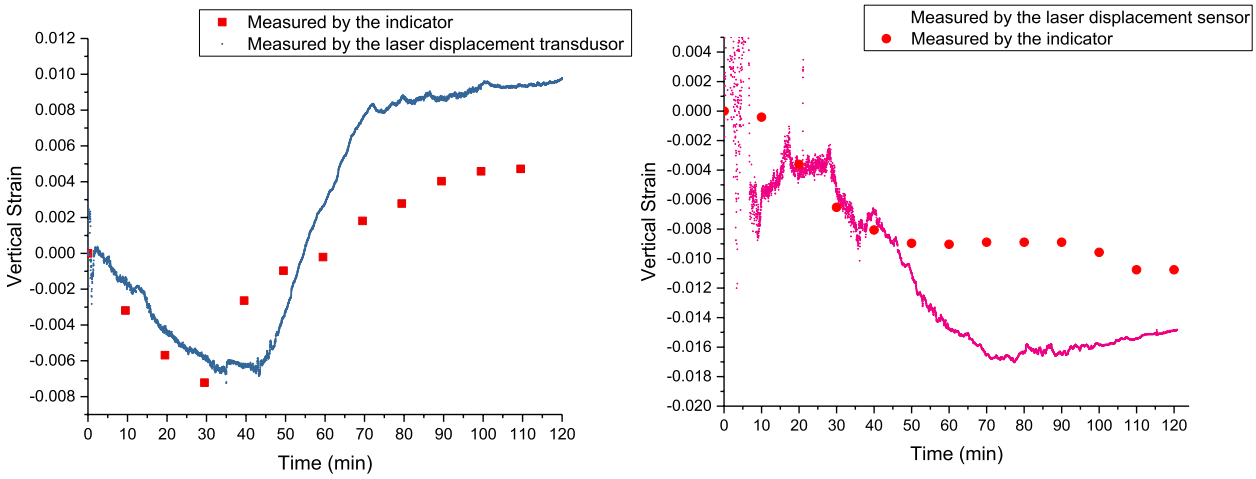

Fig. 2 Vertical volumetric strain of saturated silt specimen subjected to (**a**) freezing and (**b**) thawing

due to the compaction of matric suction, then the vertical strain of the specimen increased from −0.0065 to 0.01 for the rest of the time due to the frost heave. From Fig. 2, it is observed that the vertical strain measured by the indicator is smaller than that measured by the laser displacement transducer possibly because the tip of the dial gauge indicator applied a load to the surface of silt specimen, which decreased the vertical deformation; while the vertical strain measured by the laser was non-contact measurement and is not affected by the mechanical contact. It is also observed that the contractive vertical strain measured by the dial gauge indicator reached to the lowest value 5 minutes earlier than that measured by the laser displacement transducer. Possibly because the contact between the metal stick of the indicator and the silt specimen leads to faster rate of heat exchange and the measuring point on the silt specimen froze faster to arrive at the frozen point earlier. It was concluded that for the volume change during the freezing process, the vertical strain measured by the dial gauge indicator is probably less reliable than that measured by the laser displacement transducer.

During the thawing process, for the silt specimen measured by the indicator, the vertical strain decreased from 0 to −0.009 in the first 50 min, then, the vertical strain came to a stable level during 50 min to 90 min because the matric potential decreased which caused volume expansion counteracting the decreases in the volume due to phase change of ice. The vertical deformation continued to decrease and gradually became stable to be −0.01 for the rest of the time. For the silt specimen measured by the laser displacement sensor,

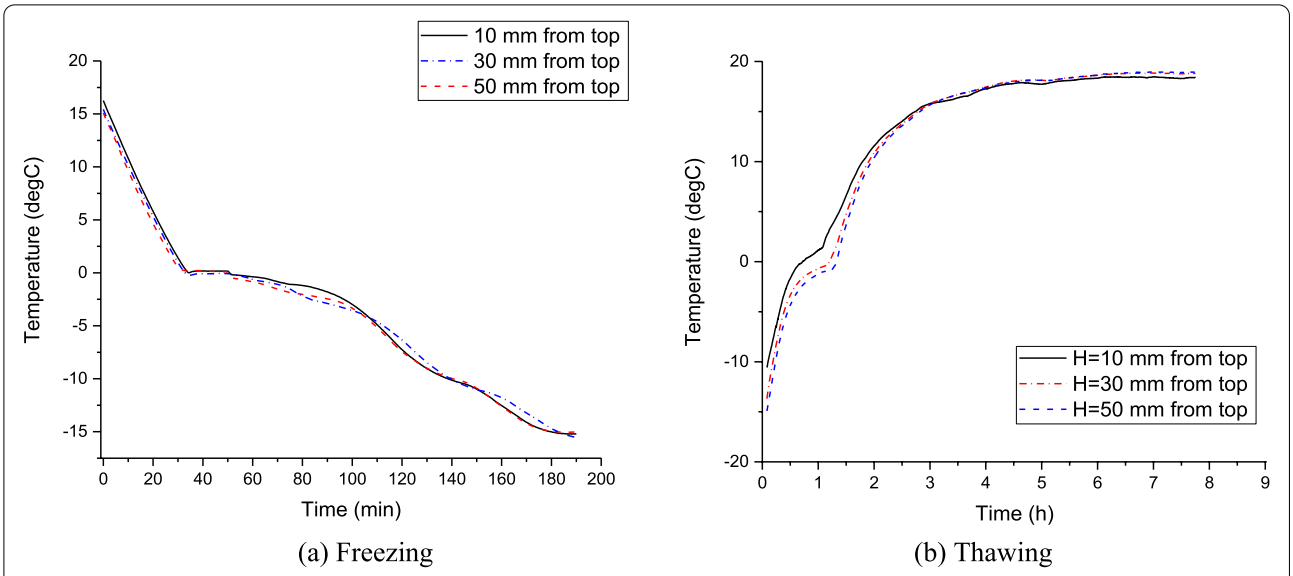

Fig. 3 Measured temperatures in saturated silt specimen subjected to (**a**) freezing, (**b**) thawing

the measured data were not stable in the first half hour. It was observed that the ice crystal exists on top of the silt specimen which is melted into water in the first half hour. It is speculated that the ice crystal melting accounts for the unstable measurement of the vertical strain. The vertical strain decreased during 30 min to 80 min of thawing due to phase change of ice. The vertical deformation became stable to be − 0.015 for the rest of the time.

Figure 3a shows the measured temperature process along the soil specimens during the freezing process. As shown in this figure, the temperature decreased fast above 0 degrees Celsius, and then it decreased at a slower rate at around 0 degrees Celsius due to the latent heat of fusion. The temperature decreased fast again below the 0 degrees Celsius and gradually approach to the temperature in the freezer. Comparing Fig. 3 and Fig. 2, it is noticed that during the phase change process (35 min to 80 min), the vertical strain of the silt specimen sharply increased due to the expansion of the ice phase.

Figure 3b shows the temperature process along the soil specimens during the thawing process. The temperature increased quickly until reaches around 0 degrees Celsius, where the temperature increases slowly due to the latent heat of fusion. After that the temperature increases fast again above 0 degrees Celsius and gradually approached the environment temperature. It took about six hours for the silt specimen to reach a thermal balance condition (i.e., the temperature of the silt specimen is the same to the environment). Since the thermal influx is from top of the silt specimen, the temperature is consistently higher at location closer to the top surface of the specimen.

Phase coded RFEM model of frozen soil

The following steps are undertaken to simulate the microstructure of frozen soils, 1) determination of volume content of different phases. The volumetric content of each phase is calculated from the physical information including the dry density, water content, and specific gravity. 2) generation of matrix for soil specimen. A m × n matrix is generated by use of Matlab, where each cell in the matrix contains the corresponding phase coding. For the dimension of the matrix, m is set to be equal to the height of the soil specimens divided by the diameter of the soil particle, while n equals to the radius of the soil specimens divided by the diameter of the soil particle. Thus, m × n equals the total number of elements in the image of a 2-D soil model specimen. 3) Phase coding of digital soil specimen. Each element in the matrix is assigned with a value to represent a particular phase of the soil specimens. Four different numbers (0, 1/3, 2/3 and 1) are assigned to represent different phases (soil particles, ice, water and air) within the soil specimens. The phase is determined by a MATLAB random number generator plus a classification statement code for each element of the m × n matrix, where the probability of occurrence of a particular phase is always same as the volumetric content of that phase in the specimen.

This process was repeated for each pixel element of the m by n matrix. Consequently, the m by n matrix contains the phase coding that represent the volume proportion of different phases, which can be visually shown as a grey scale image. Each pixel of the image represents an element in the soil matrix, with the color of the pixel corresponding to the type of the phase. Four different colors

(black, dark grey, light grey, and white) represent the soil particles, ice, water and air, respectively. With the procedure described, the probability of occurrence or the percentage of each phase is approximately equal to the volumetric content of each phase when the m by n matrix is sufficiently large. The image is saved and subsequently read as input by a multiphysics platform COMSOL@.

The microstructure image is imported to the finite element software code COMSOL@, which leads to phase coded image with slightly different phase code (dark blue, light blue, yellow, and red represent the soil particles, ice, water and air, respectively). COMSOL is used since it allows to assign the material properties based on the color scale of the image. Figures 4 shows the 2-D phase coded image of the silt specimen at different degrees of thawing (or freezing) in Matlab and in Comsol.

With the microstructure based random FEM model, the multiphysical parameters (including thermal, mechanical, hydraulic) can be assigned to each pixel based on the phase code of the image. Therefore, the properties at each pixel are based on the intrinsic property of the phase of the material at that location. Following this method, the heat capacity, thermal conductivity, and density of the air, water, ice, and silt particles are assigned to each pixel based on the phase code of the silt specimen. The mechanical parameters can also be assigned to each phase based on the microstructure of random FEM. The Young's modulus, Poisson's ratio, density, and volumetric coefficient of thermal expansion of the air, water, ice, and silt particles (Table 1) are assigned to each pixel based on the color phase code corresponding to different phases in the silt specimen. The thermal properties of water are modelled with a non-constant value to account for the volume change during phase transition (9% of volume expansion when water freeze into ice). The properties of each phase are summarized by referring Bejan and Kraus [36] and shown in Table 1.

2-D axisymmetric model for the silt specimen is constructed with the phase coding described. Once the RFEM is build, the boundary conditions are applied based on experimental conditions. To simulate the behaviors of the temperature distribution during the thawing process, thermal insulations are applied on sides and the bottom of the 2-D axisymmetric silt model. The initial temperature of the silt specimen is set to be −20 degrees Celsius. A boundary temperature of 19 degrees Celsius is applied on top of the model to initialize the thawing process. To simulate the mechanical behavior of the specimen, a fixed boundary was added in the bottom of the speciemn to control its displacement.

Figure 5 compares the temperature process predicted by the RFEM model simulation and the corresponding experimental measurement at different heights of the silt specimen during the thawing process. In general, the results by the RFEM model simulation agrees very well with the experimental measurement, which validates the reliability of this newly developed microstructure based random finite element model. Both experimental data and computational model show that it takes about 6 hours for the silt to reach a thermal balance condition with the surrounding environment.

To simulate the production of internal stress during the freezing process, a simulation case is designed where thermal insulations are applied on the sides and the bottom of the 2-D unfrozen silt model. The initial temperature of the silt specimen is set to 20 degrees Celsius. The

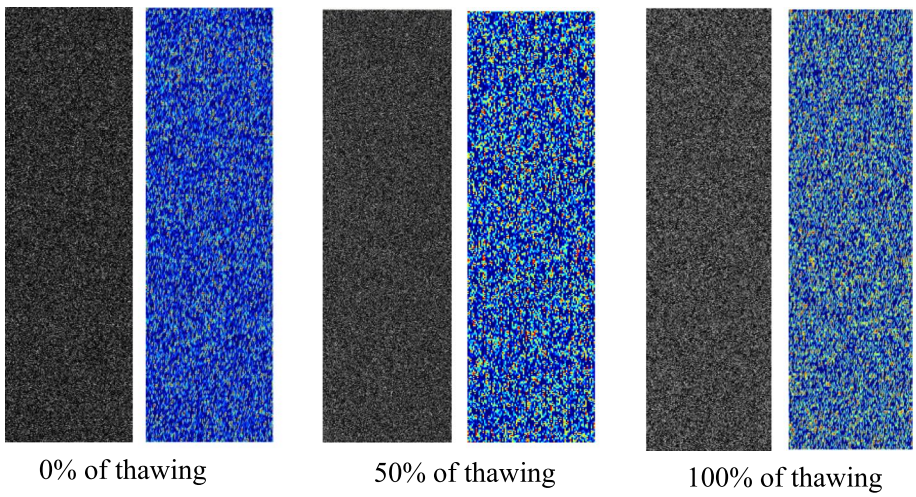

Fig. 4 Phase coded microstructure-based image for silt sample with different degrees of thawing (the gray-scale image is phase coded in Matlab, the color image is phase coded after conversion into Comsol)

Table 1 Parameters used for the random FEM model simulation

Constant	Value	Units	Description
W	10	m	Horizontal distance of the study region
$D_{asphalt}$	0.2032	m	Thickness of the asphalt layer
D_b	0.1524	m	Thickness of the base layer
D_s	1	m	Thickness of the silt layer
w	0.15	1	Initial water content
ρ	1708	kg/m^3	Dry density of silt specimen
d	50	μm	Diameter of silt particle
G_s	2.65	1	Specific gravity of silt specimen
E_s	12.7	GPa	Young's modulus of silt particle
E_i	9	GPa	Young's modulus of ice
E_w	3.9×10^{-5}	Pa	Young's modulus of water
E_a	0	Pa	Young's modulus of air
$E_{asphalt}$	9	GPa	Young's modulus of the asphalt layer
E_b	0.3	GPa	Young's modulus of the base layer
E_{ps}	3	GPa	Young's modulus of the polystyrene foam
E_{pu}	0.1	GPa	Young's modulus of the polyurethane foam
E_{gf}	10	GPa	Young's modulus of the glass fiber board
μ_s	0.3	1	Poisson's ratio of silt particle
μ_i	0.3	1	Poisson's ratio of ice
μ_w	0.5	1	Poisson's ratio of water
μ_a	0	1	Poisson's ratio of air
$\mu_{asphalt}$	0.35	1	Poisson's ratio of the asphalt layer
μ_b	0.3	1	Poisson's ratio of the base layer
μ_{ps}	0.4	1	Poisson's ratio of the polystyrene foam
μ_{pu}	0.32	1	Poisson's ratio of the polyurethane foam
μ_{gf}	0.25	1	Poisson's ratio of the glass fiber board
ρ_s	2600	kg/m^3	Density of silt particle
ρ_i	917	kg/m^3	Density of ice
ρ_w	1000	kg/m^3	Density of water
ρ_a	1.29	kg/m^3	Density of air
$\rho_{asphalt}$	2243	kg/m^3	Density of the asphalt layer
ρ_b	1680	kg/m^3	Density of the base layer
ρ_{ps}	46	kg/m^3	Density of the polystyrene foam
k_s	2	W/m·K	Thermal conductivity of silt particle
k_i	2.2	W/m·K	Thermal conductivity of ice
k_w	0.58	W/m·K	Thermal conductivity of water
k_a	0.025	W/m·K	Thermal conductivity of air
$k_{asphalt}$	0.75	W/m·K	Thermal conductivity of asphalt layer
k_b	0.7	W/m·K	Thermal conductivity of base layer
k_{ps}	0.03	W/m·K	Thermal conductivity of the polystyrene foam
Cp_s	835	J/kg·K	Heat capacity of silt particle
Cp_i	1960	J/kg·K	Heat capacity of ice
Cp_w	4181.3	J/kg·K	Heat capacity of water
Cp_a	1005	J/kg·K	Heat capacity of air
$Cp_{asphalt}$	920	J/kg·K	Heat capacity of the asphalt layer
Cp_b	840	J/kg·K	Heat capacity of the base layer
Cp_{ps}	1500	J/kg·K	Heat capacity of the polystyrene foam
Cp_{pu}	1450	J/kg·K	Heat capacity of the polyurethane foam
L_f	334	kJ/kg	Latent heat fusion of water

Table 1 (continued)

Constant	Value	Units	Description
α_s	9×10^{-6}	1/K	Volumetric coefficient of thermal expansion of silt particle
α_i	1.9×10^{-4}	1/K	Volumetric coefficient of thermal expansion of ice
α_w	2.07×10^{-4}	1/K	Volumetric coefficient of thermal expansion of water
α_a	3.43×10^{-3}	1/K	Volumetric coefficient of thermal expansion of air
$\alpha_{asphalt}$	4×10^{-5}	1/K	Volumetric coefficient of thermal expansion of the asphalt
α_b	4×10^{-5}	1/K	Volumetric coefficient of thermal expansion of the base layer
α_{ps}	7×10^{-5}	1/K	Volumetric coefficient of thermal expansion of the foam
α_{pu}	6.5×10^{-5}	1/K	Volumetric coefficient of thermal expansion of the polyurethane foam
α_{gf}	3×10^{-5}	1/K	Volumetric coefficient of thermal expansion of the glass fiber board

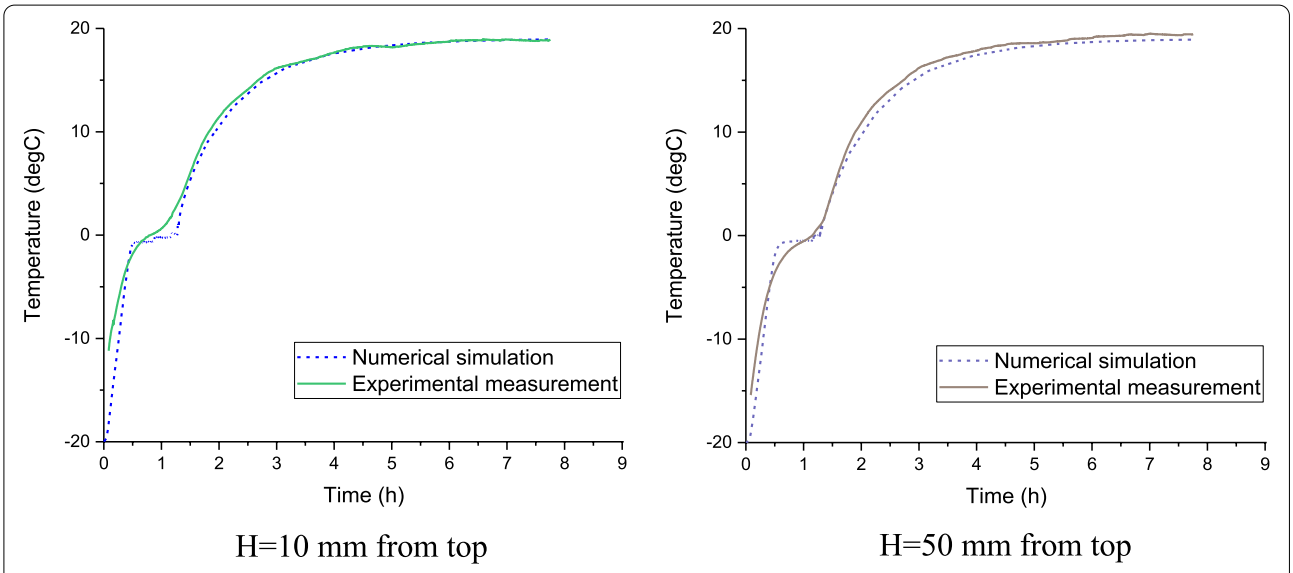

Fig. 5 Comparison of the temperature process at different heights in the specimen during the thawing process by RFEM simulation and experimental measurement

boundary temperature of −20 degrees Celsius is applied on top surface of the model to start the freezing process. Under such conditions, the internal stress is generated by the development of matric suction and thermal expansion due to water/ice phase transition. Fig. 6 plots the characteristics of internal stress distribution in the cross sections at different heights of the silt specimen. As can be seen from this Figure, the internal shear stress is not uniform along the specimen. Instead, it is higher at locations closer to the surface of the soil. After 6 hours, when achieving the thermal balance condition, the internal shear stress is more uniformly distributed. For each cross section, the stress is not uniform and show statistical nature. The simulation results reveal that the microstructure of the soil have important influence on the internal stress development in soil subjected to freezing. The observation that the average internal stress decreases with depth into the specimen is consistent with the results by the continuous homogenized model by Liu and Yu [37].

Analysis of soil freezing effects on pavement with RFEM model

To demonstrate the engineering applications of the new model, it is also utilized to analyze the interactions between subsoil and pavement surface subjected to freezing conditions. The dimension and the mesh of the pavement structure is illustrated in Fig. 7. The pavement structure includes 20.32 cm of asphalt layer, 15.24 cm base layer, 7.62 cm polystyrene insulation layer, and underlain with 1 m of subgrade soils. The pavement top boundary and lower boundary are 8 m and 10 m in

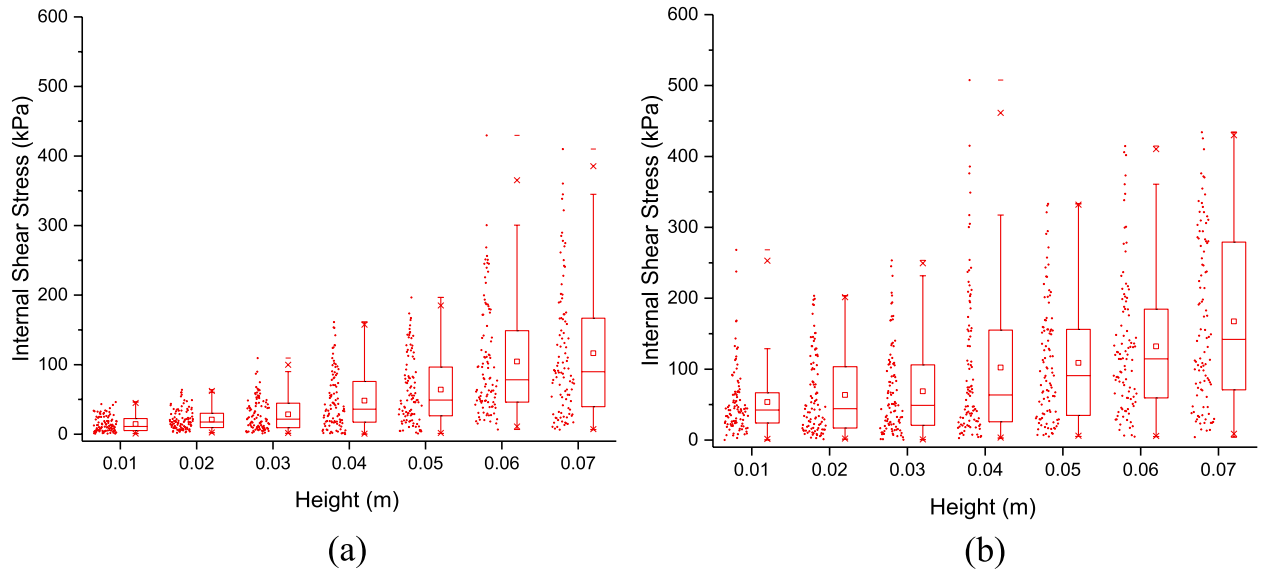

Fig. 6 Box chart of the distribution of the internal shear stress (kPa) along the height of soil specimen during the freezing process. **a** 10 minutes; **b** one hour. (The square in the center of each box indicates the mean value of the internal stress. The horizontal line inside each box is the median value of the internal stress. The upper and lower bounds of the box are determined by 75th and 25th percentiles. The whiskers are determined by the 95th and 5th percentiles)

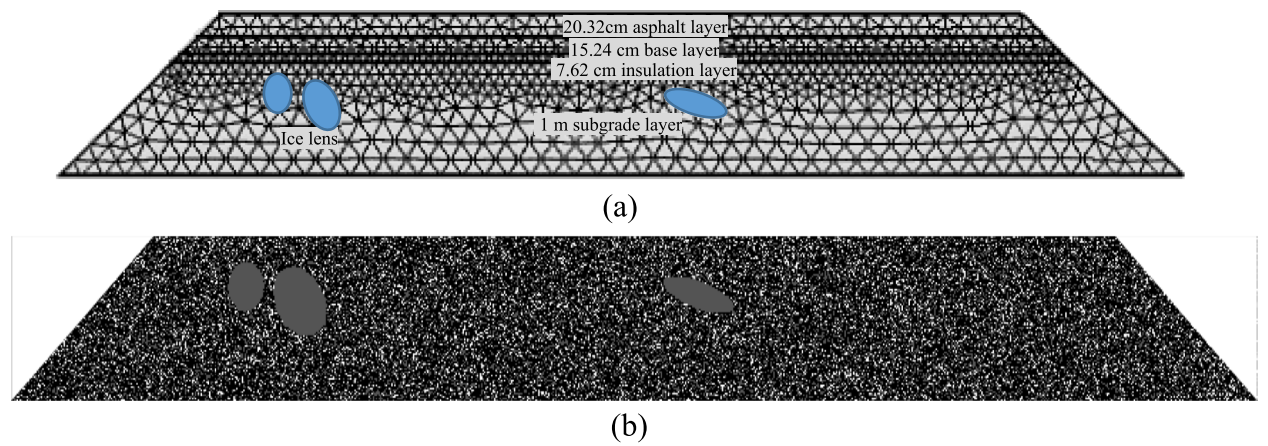

Fig. 7 **a** Mesh of the pavement structure; **b** Phase coded model in subgrade layer

width, separately. The subgrade is assumed to be silty soil measured in the lab experiments. The similar phase compositions are used to characterize the randomness in the subsoil layer. Ice lenses are assumed to randomly develop in the subgrade layer (Fig. 7). The parameters of materials for the pavement structure are listed in Table 1.

For the thermal boundary conditions, thermal insulation boundary conditions are applied at the bottom of the pavement subgrade. Heat flux boundary conditions are applied on sides and on top of the pavement. The initial temperature of the study region is set to −15 degrees Celsius. The boundary temperature applied on top and sides of the pavement are set to the daily average temperature of 2017 at Anchorage, Alaska (Fig. 8a). The daily heat transfer coefficent (Fig. 8b) is calculated from the daily average wind speed of 2017 at Anchorage, Alaska. For the mechanical boundary conditions, the roller constraint is applied at the bottom of the subgrade layer. And the fixed point constraint is applied at the bottom right corner of the subgrade layer to restrain the rigid body movements.

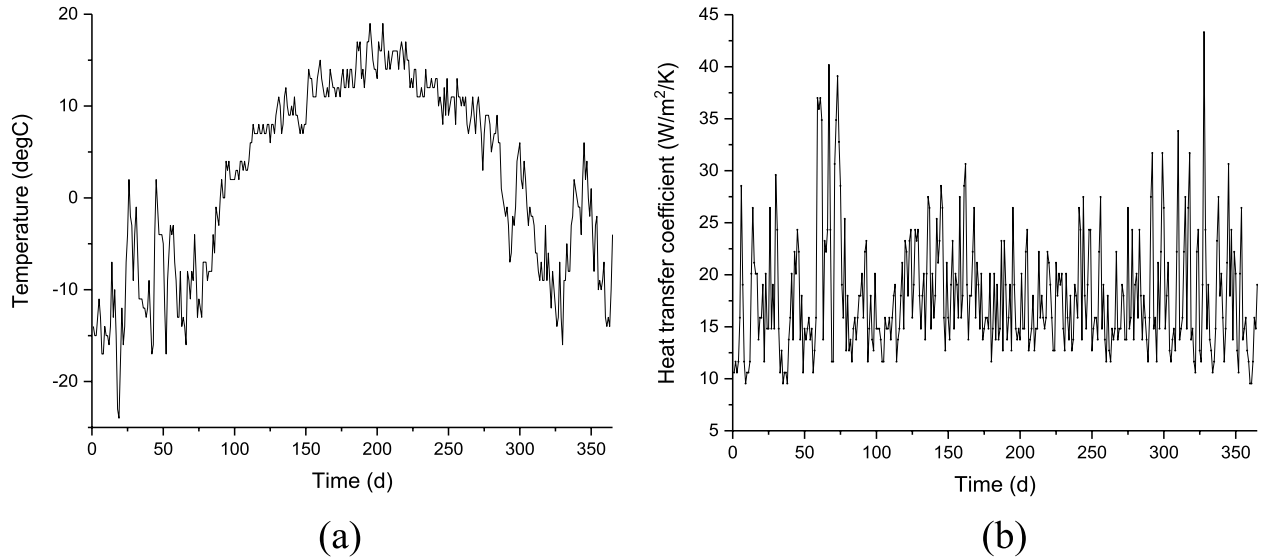

Fig. 8 Average daily (a) temperature; (b) ground heat transfer coefficent in 2017 at Anchorage, Alaska

Computational model is implemented with the RFEM model and pavement structure is subjected to ground freezing. The existing of ice lenses and the expansion of soils leads to development of tensile stress in the pavement structure as well as non-uniform frost heave. Fig. 9 summarizes the results of tensile stress and vertical displacement distribution on the surface of asphalt layer, base layer and subgrade layer on March 1st, 2017 at Anchorage, Alaska. The results indicate that there are appreciable amount of tensile stress developed in the pavement structure as the results of frost heave. After 60 days of freezing, frost heave leads to development of tensile stress and vertical displacement in the pavement structure. For example, the maximum tensile stress is 5.2 MPa on the surface of asphalt layer. The maximum vertical displacement in the asphalt layer reaches 14.7 mm. It is interesting to notice that the maximum stress and deformation on asphalt layer surface are located at the postion where the largest ice lens is underneath in the subgrade soil, which indicates that ice lens formation is a major factor for frost heave and deterieration in the pavement. It is also worth noted that the

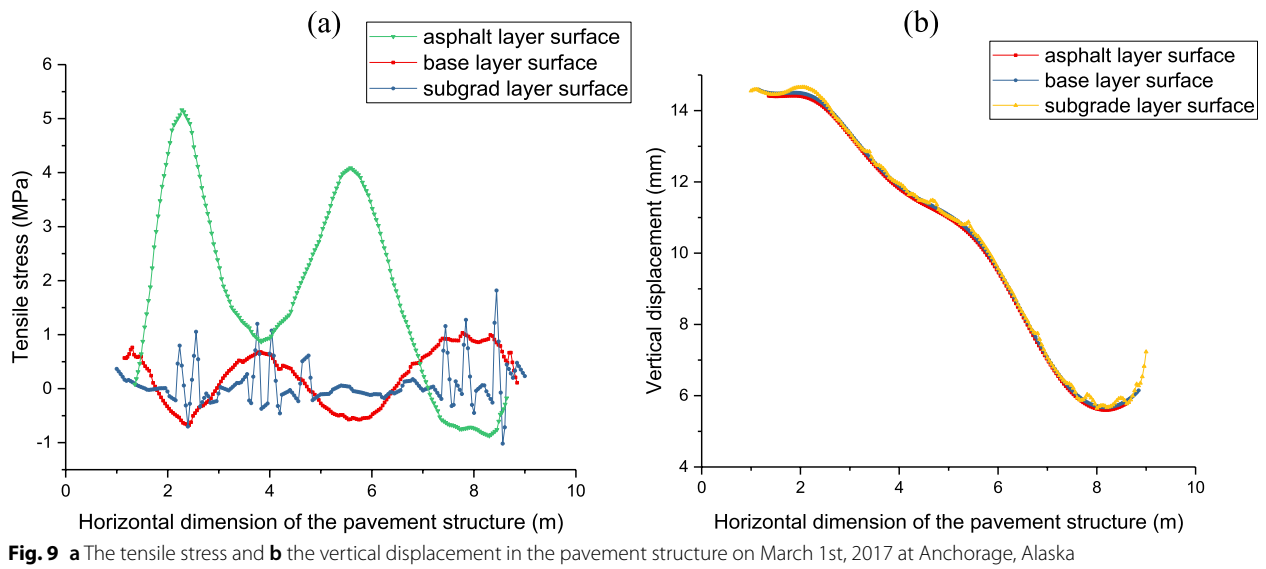

Fig. 9 **a** The tensile stress and **b** the vertical displacement in the pavement structure on March 1st, 2017 at Anchorage, Alaska

stress and deformation on the subgrade layer surface is less continous as those on base layer surface and asphalt layer surface. It is due to the microstructure and discrete nature of the subgrade soil.

Thermally insulated pavement is used in pavement specifications in a few Northern European countries (i.e., Finland, Sweden, Norway) and Canada. To analyze the effects of pavement insulation, simulations are conducted on the pavement structure underlain by a 7.62 cm polystyrene foam insulation layer between the base layer and the subgrade. The results are summarized in Fig. 10. The results show that the use of pavement insulation layer is effective in mitigating the stress and frost heave development in the pavement structure. For example, the maximum tensile stress and vertical displacement on the asphalt layer surface with the insulation foam are 1.5 MPa and − 1.6 mm ('-' indicates contraction), respectively. Both are significant less than the maximum tensiles stress (5.2 MPa) and vertical displacement (14.7 mm) on the surface of asphalt layer of the pavement structure without insulation foam.

Other types of thermal insulation materials, such as polyurethane and glass fiber board are applied in the simulation to study their mitigation effects on pavement deteriaration. The results are summarized in Fig. 11 and Fig. 12. The results show that both insulation materials are effective in mitigating the stress and frost heave in the pavement structure. For example, the maximum tensile stress and vertical displacement on the asphalt layer surface with the polyurethane insulation foam are 1.3 MPa and − 1.1 mm ('-' indicates settlement), respectively. All these thermal insulation measures are effective in reducing the stresses in pavement strcutrue and mitigate fround heave. The cost and effectiveness of three different insulation materials are compared and summarized in Table 2.

Reducing the water content in the subgrade soil by proper drainage measures is another method for mitigating the frost heave. To analyze the effect of drainage, simulations are conducted with different degrees of satuation in the subgrade layer. The results are summarized in Fig. 13. The results show that decreasing the saturation in subgrade soil is effective in reducing the stress and deformation in the pavement structure. For example, the maximum tensile stress decreased from 3.75 MPa to 2.52 MPa by reducing the saturation of subgrade soil from 100% to 80%, while the maximum vertical displacement decreased from 10.5 mm to 7.2 mm in the meantime.

The simulation results indicate that the use of thermal insulation layer or improveing drainage of subgrade soil are both effective to mitigate the stress development and frost heave in cold region pavement. Other solutions for mitigating the frost heave of pavement is through subgrade soil improvement, for example, via cement or lime treated subgrade.

Conclusion

A microstructure-based random finite element simulation model is developed to simulate frost heave in soils and consequently to study its engineering impacts. This model is able to simulate the bulk behaviors of frozen soils by considering the microstructures, including frost

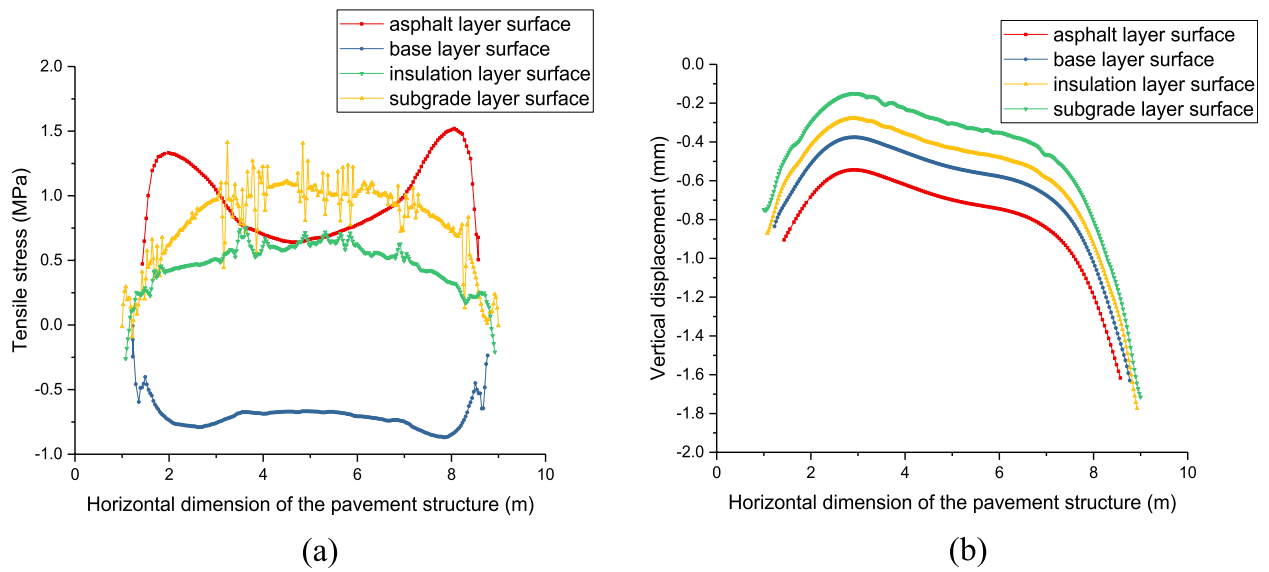

Fig. 10 a The tensile stress and **b** the vertical displacement in the pavement structure with polystyrene insulation layer on March 1st, 2017 at Anchorage, Alaska

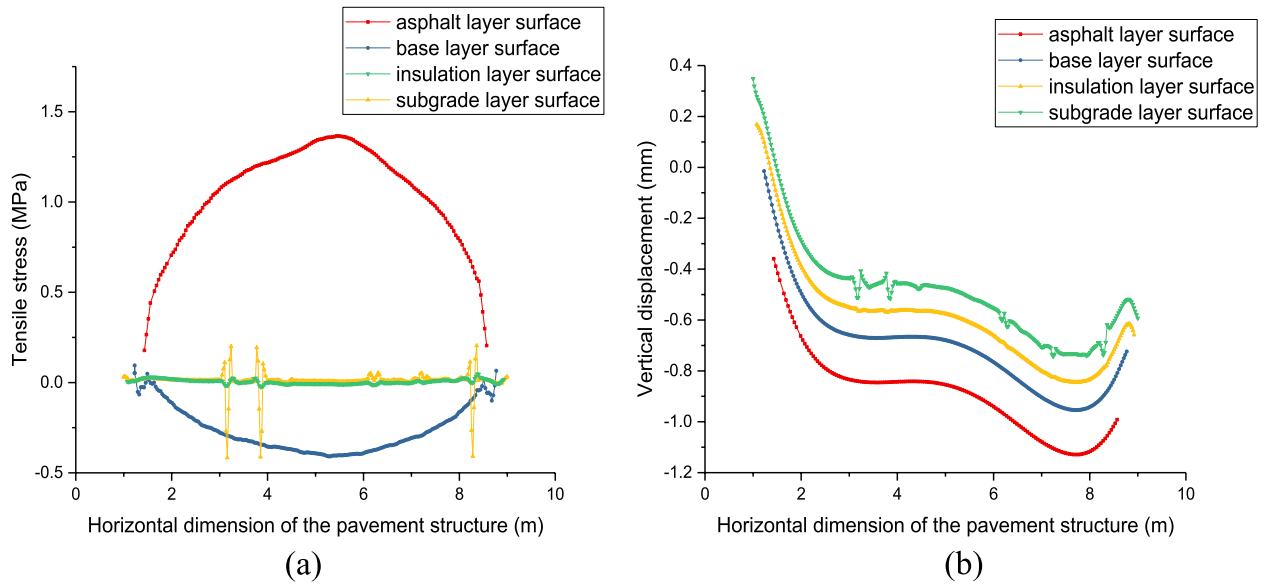

Fig. 11 **a** The tensile stress and **b** the vertical displacement in the pavement structure with polyurethane insulation layer on March 1st, 2017 at Anchorage, Alaska

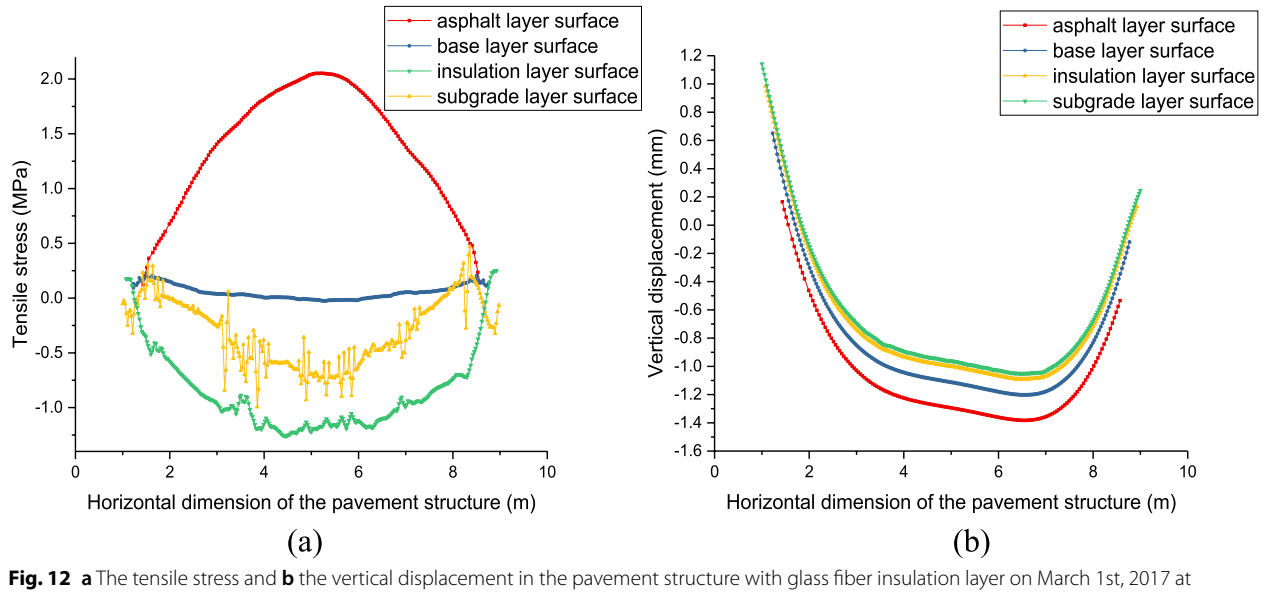

Fig. 12 **a** The tensile stress and **b** the vertical displacement in the pavement structure with glass fiber insulation layer on March 1st, 2017 at Anchorage, Alaska

Table 2 The cost and effectiveness of the insulation materials

Insulation material	Cost (USD/m^3)	Maximum tensile stess in asphalt layer (MPa)	Maximum displacement in asphalt layer (mm)
No	N/A	5.1	14.6 mm
polystyrene	72–131	1.5	−1.6
polyurethane	100–300	1.3	−1.1
glass fiber board	45–60	2.0	−1.4

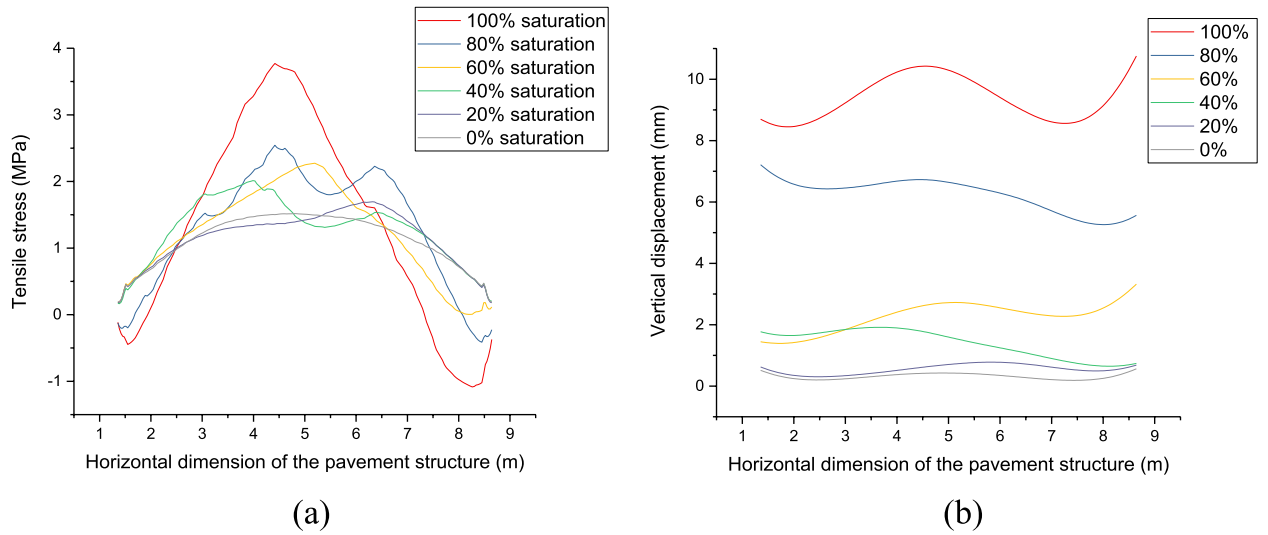

Fig. 13 **a** The tensile stress and **b** the vertical displacement on the surface of asphalt layer with different degrees of saturation in the subgrade layer on March 1st, 2017 at Anchorage, Alaska

induced volume change and development of internal stress. The results of computational model is validated by experimental data. The model is utilized to analyze the effects of ground freezing on the pavement structures. The model is able to simulate the frost heave of subgrade soil, which causes the development of internal stress in pavement structure due to frost heave. This RFEM model simulation is also conducted on the mitigation strategies. The results unveil the benefits of applying thermal insulation layer or drainage of subsoil layer to mitigate the magnitudes of ground heave under the pavement structure as well as the induced internal stresses. Overall, the random finite element method provides holistical simulation of pavement responses to freezing conditions by accounting for the spatial non-homogeneity of soils and coupled thermo-mechanical processes.

Acknowledgements
The authors acknowledge Jim Berilla for assistance with experimental design. We appreciate the US National Science Foundation for support of this research.

Authors' contributions
Shaoyang Dong: produce simulation model, conduct experiment, draft the manuscript; Yusheng Jiang: refine the simulation model, refine the manuscript; Xiong Yu: envision the study. The author(s) read and approved the final manuscript.

Funding
The research is partially supported by the US National Science Founation.

Availability of data and materials
Data available upon request from the correspondence author. The following datasets related to work presented are available upon request: experimental data of soil volume and temperature evolution subjected to freezing/thawing process that is used to validate the computational model, code for generation of random soil sample.

Declarations

Ethics approval and consent to participate
Yes

Consent for publication
Yes

Competing interests
No

Author details
[1]Graduate Research Assistant, Department of Civil and Environmental Engineering, Case Western Reserve University, Cleveland, OH, USA. [2]Opal J. and Richard A. Vanderhoof Professor and Chair, Department of Civil and Environmental Engineering, Professor of Electrical Engineering and Computer Science, Case Western Reserve University, Cleveland, OH, USA.

Received: 15 April 2022 Revised: 1 September 2022 Accepted: 12 October 2022
Published online: 21 November 2022

References

1. Janoo VC, Berg RL (1990) Thaw weakening of pavement structures in seasonal frost areas. Trans Res Rec 1286:217–233
2. Roy M, Crispin J, Konrad JM, Larose G (1992) Field study of two road sections during a freeze-thaw cycle. Trans Res Rec 1362:71–78
3. Doré G, Konrad JM, Roy M (1997) Role of deicing salt in pavement deterioration by frost action. Trans Res Rec 1596:70–75
4. Doré G (2002) Cold region pavement. J Glaciol Geocryol 24(5):593–600
5. Schaus, L., Eng, P., Popik, M., & Eng, M. Frost heaves: a problem that continues to swell. In 2011 Conference and exhibition of the transportation Association of Canada. Transportation Successes: Let's Build on Them. , 2011
6. Zhang K, Kevern J (2021) Review of porous asphalt pavements in cold regions: the state of practice and case study repository in design, construction, and maintenance. J Infrastructure Preserv Resilience 2(1):1–17
7. Oswell JM (2011) Pipelines in permafrost: geotechnical issues and lessons. Can Geotech J 48(9):1412–1431
8. Li N, Chen B, Chen F, Xu X (2000) The coupled heat-moisture-mechanic model of the frozen soil. Cold Reg Sci Technol 31(3):199–205

9. Neaupane KM, Yamabe T (2001) A fully coupled thermo-hydro-mechanical nonlinear model for a frozen medium. Comput Geotech 28(8):613–637
10. Liu Z, Yu XB, Tao JL, Sun Y (2012) Multiphysics extension to physically based analyses of pipes with emphasis on frost actions. J Zhejiang University-Science A 13(11):877–887
11. Zhou MM, Meschke G (2013) A three-phase thermo-hydro-mechanical finite element model for freezing soils. Int J Numer Anal Methods Geomech 37(18):3173–3193
12. Zhang Y, Michalowski RL (2015) Thermal-hydro-mechanical analysis of frost heave and thaw settlement. J Geotech Geoenviron 141(7):04015027
13. Ji Y, Zhou G, Zhou Y, Hall MR, Zhao X, Mo P (2018) A separate-ice based solution for frost heaving-induced pressure during coupled thermal-hydro-mechanical processes in freezing soils. Cold Reg Sci Technol 147:22–33
14. Wu Y, Zhai E, Zhang X, Wang G, Lu Y (2021) A study on frost heave and thaw settlement of soil subjected to cyclic freeze-thaw conditions based on hydro-thermal-mechanical coupling analysis. Cold Reg Sci Technol 188:103296
15. Brownell DH, Garg SK, Pritchett JW (1977) Governing equations for geothermal reservoirs. Water Resour Res 13(6):929–934
16. Rabin Y, Steif PS (1998) Thermal stresses in a freezing sphere and its application to cryobiology. J Appl Mech 65(2):328–333
17. MacKay MH, Hein DK, Emery JJ (1992) Evaluation of frost action mitigation procedures for highly frost-susceptible soils. Trans Res Rec 1362:79–89
18. Doré G, Konrad JM, Roy M (1999) Deterioration model for pavements in frost conditions. Trans Res Rec 1655:110–117
19. Niu F, Zheng H, Li A (2020) The study of frost heave mechanism of high-speed railway foundation by field-monitored data and indoor verification experimen. Acta Geotech 15(3):581–593
20. Taber S (1930) The mechanics of frost heaving. J Geol 38(4):303–317
21. Miller RD (1972) Freezing and heaving of saturated and unsaturated soils. Highw Res Rec:393
22. Style RW, Peppin SS, Cocks AC, Wettlaufer JS (2011) Ice-lens formation and geometrical supercooling in soils and other colloidal materials. Phys Rev E 84(4):041402
23. Bharrucha-Reid AT (ed) (1968) Probabilistic methods in applied mathematics. Academic Press, New York
24. Fenton GA, Griffiths DV (2003) Bearing-capacity prediction of spatially random c φ soils. Can Geotech J 40(1):54–65
25. Johari A, Gholampour A (2018) A practical approach for reliability analysis of unsaturated slope by conditional random finite element method. Comput Geotech 102:79–91
26. Johari A, Talebi A (2021) Stochastic analysis of piled-raft foundations using the random finite-element method. Int J Geomechanics 21:04021020
27. Sobczyk K (1985) Wave propagation in random media. Elsevier, New York
28. Fenton GA, Griffiths DV, Williams MB (2005) Reliability of traditional retaining wall design. Geotechique 55(1):55–62
29. Luo N, Bathurst RJ (2018) Probabilistic analysis of reinforced slopes using RFEM and considering spatial variability of frictional soil properties due to compaction. Georisk 12:87–108
30. Selmi M, Kormi T, Hentati A, Ali NBH (2019) Capacity assessment of offshore skirted foundations under HM combined loading using RFEM. Comput Geotech 114:103148
31. Andersland OB, Ladanyi B (2004) Frozen ground engineering. Wiley, Hoboken, NJ
32. Chang CS, Hicher PY (2005) An elasto-plastic model for granular materials with microstructural consideration. Int J Solids Struct 42:4258–4277
33. Ferber V, Auriol J, Magnan J, Cui Y, De Laure E, Gerente C (2006) A microstructural model for the volume changes of unsaturated siltey soils due to wetting. Unsaturated Soils:861–872
34. Tracy SR, Daly KR, Sturrock CJ, Crout NMJ, Mooney SJ, Roose T (2015) Three-dimensional quantification of soil hydraulic properties using X-ray computed tomography and image-based modeling. Water Resour Res 51(2):1006–1022
35. Helliwell JR, Sturrock CJ, Grayling KM, Tracy SR, Flavel RJ, Young IM et al (2013) Applications of X-ray computed tomography for examining biophysical interactions and structural development in soil systems: a review. Eur J Soil Sci 64(3):279–297
36. Bejan, A, & Allan D. K. Heat transfer handbook. 1. Wiley, 2003
37. Liu Z, Yu X (2011) Coupled thermo-hydro-mechanical model for porous materials under frost action: theory and implementation. Acta Geotech 6(2):51–65
38. Doré G, Flamand M, Tighe S (2001) Prediction of winter roughness based on analysis of subgrade soil variability. Trans Res Rec 1755:90–96

Publisher's Note